Cake formation in the filtration of associative microgel suspensions

Swati Kaushik, Steven Meeker, Guillaume Ovarlez

Cake formation in the filtration of associative microgel suspensions

Swati Kaushik, Steven Meeker, Guillaume Ovarlez

Univ. Bordeaux, CNRS, Syensqo, LOF, UMR 5258, F-33600 Pessac, France

In this work, we investigate the jamming behavior of associative microgel suspensions used as fluid loss additives in model porous media. We first construct a phase diagram using drying experiments, followed by characterization of the suspensions' rheology and the permeability of the filter cakes at maximum microgel concentration. Microfluidic devices are designed for frontal and lateral flow filtration with pore sizes comparable to or slightly larger than the microgel particles. Microscopic observations reveal irreversible aggregation as the particles pass through pores, leading to cake formation inside and at the exit of the pores—contrary to the classical view of cake formation. Flow in linear channels of similar pore size, however, does not cause jamming, suggesting that extensional shear plays a crucial role. We hypothesize that extensional flows promote the association of hydrophobic groups by unfolding dangling chains, resulting in low-permeability filter cakes with self-adaptive properties for larger pore networks.

Topical area: Transport Phenomena and Fluid Mechanics.

Keywords: microgel suspensions, fluid loss, filter cake, porous media, microfluidics.

1. Introduction

Recovery of oil and gas from porous rocks is a complex process, since oil is extracted from rock formations located miles below the surface of the Earth, where temperature and pressure are very high[1]. One of the main challenges is to prevent uncontrolled leakage of oil or gas at any moment, as this could have a significant impact on both the operating crews and the surrounding environment. The highest risk of leakage occurs during the construction of the well, as the borehole is drilled through multiple formation layers with varying porosity, fluid composition, pore pressures, and temperature. In general, during the construction of a well, a hydraulic overpressure (relative to the pore pressure) is applied to the open hole section to prevent any splintering or blowout of the formation. Consequently, in order to maintain equilibrium, it is necessary to prevent leakage of the operating fluids (drilling mud, cement slurry, or completion fluid) to the formation.

Fluid loss control additives are of paramount importance in both drilling and cementing operations, constituting a vital component of the fluid formulation. These additives are designed to ensure that the base fluid remains within the wellbore and to prevent invasion into the surrounding rock formation while the fluid is pumped under high differential pressure across the rock. In the context of cementing, these additives serve to retain water within the slurry, thus ensuring its availability for the cement setting. At the initial stages of fluid placement or circulation along the formation, an impermeable filter cake is formed through a tangential filtration process. The filter cake may be classified as either "external" or "internal." An external filter cake is located on the surface of the formation and consists primarily of fluid loss additives and solids present in the fluid, including bentonite, barite, and cement. On the contrary, an internal filter cake forms within the first few millimeters of the rock formation, which is plugged by the penetration of the fluid loss additive into its pores. Once the filter cake is formed, ideally with minimal loss of fluid, the wellbore remains stable and further filtration is significantly limited.

During the past 30 years, there has been a growing interest in the utilization of novel chemical polymeric products as fluid loss additives. This growing interest lies in the necessity to replace toxic and non-ecofriendly chemicals and in the increasing technical challenges associated with the exploitation of unconventional resources, such as shale gas or shale oil.

These additives may be classified into two main categories. One is based on linear polymers that, through interaction with suspended solids, serve to seal the porosity of the filter cake. The second category consists of additives based on particles such as colloidal latexes, prehydrated cross-linked starches, or synthetic microgels. Microgels are solvent-swollen chemically cross-linked polymers that exist as soft particles in suspension in a continuous medium – here, water[2]. In the oil and gas industry, these additives can be used for a variety of purposes, including water shutoff, modification of relative permeability, control of rheology, and fluid loss control[3-8]. In the context of fluid loss control, microgels are typically regarded as a means of plugging rock pores through the deformation of the soft cross-linked particles. These particles may penetrate the pores of rock formations to obstruct their throats. In applications as fluid loss additives, the size of the particles is often tailored to the target porosity to achieve the desired plugging effect. Figure 1 shows a schematic of the fluid loss control.

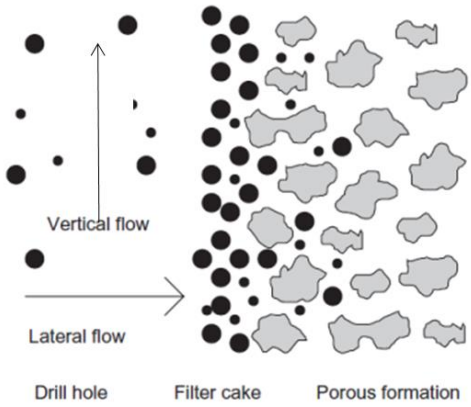

Figure 1. Schematic showing the flow along a porous formation of a fluid containing fluid loss additives, in both vertical and lateral directions, resulting in the formation of a filter cake (Image reproduced with permission from Johannes Fink, Petroleum Engineer's Guide to Oil Field Chemicals and Fluids (Second Edition), Gulf Professional Publishing, 2015, Copyright © 2015 Elsevier Inc. All rights reserved).

Microgel suspensions are typically non-Newtonian fluids when sufficiently concentrated, i.e., their viscosity may depend on the shear rate or the shear-rate history, which results from deformation and rearrangement of the soft particles. Compared to other suspensions[9], the complexity in the rheology of microgel suspensions arises from changes in the volume, deformation, and porosity of the particles, due to physiochemical changes and mechanical forces[10-12]. Their responsiveness to their external environment is also one of their main interests, as it allows one to change the rheology of microgel suspensions on demand by changing the temperature, pH, or by adding ions to the solvent[8,10,13].

The main parameters that govern the rheological properties of soft microgel suspensions are particle size, particle volume fraction, particle surface charge, and their internal structure (e.g., cross-linking density). At low concentrations, the particles are dispersed in the solvent, resulting in an increase in its viscosity. At concentrations exceeding a critical threshold, microgel suspensions exhibit properties akin to those of soft glasses, characterized by an amorphous structure. This is due to the close proximity of the particles, which impedes their movement sterically. The particle volume fraction can then be increased above the jamming concentration of similar hard particles, as the particles are deformable[14]. Microgel suspensions at high solid content show high shear viscosity and shear-thinning behavior in both the soft glassy and jamming regimes, and exhibit a yield stress above the jamming fraction.

The present study investigates the properties of hydrophilic microgels comprising associative moieties. The resulting attractive interactions are intended to enhance the capacity to form

aggregates when required and to improve the fluid loss control properties. Examples of associative polymers include amphiphilic polymers consisting of a hydrophilic backbone bearing a few hydrophobic units. These are well known to develop associative behavior when they reach a critical overlap concentration[15,16]. The development of polymer-polymer physical associations from 'sticky' hydrophobic unit interactions dramatically increases the fluid viscosity, up to the formation of gels, and has found numerous applications in the industrial and personal care industries.

Understanding the flow and filtration of complex fluids in porous media represents a significant challenge with implications in a diverse array of engineering applications. At the laboratory scale, a variety of porous media analogs have been employed, including sand beds and packed spheres. In the case of viscoelastic fluids, a significant increase in flow resistance was observed compared to Newtonian fluids[17-19]. This was attributed to extensional flows within the porous media[20-23]. Indeed, at the local scale, there is a combination of shear and extensional flows, with a particularly strong shear flow near the walls and a strong extensional flow away from the walls. This is a consequence of the converging and diverging nature of the porous media. In order to gain insight into the complex processes that occur at the pore scale, it is necessary to visualize directly the phenomena taking place inside the porous media. This has led to the development of porous material micromodels that can be manufactured using techniques such as glass micromachining[24], hydrophilic etching[25], or soft lithography.

The early work of Wyss *et al*.[26] illustrated that model microfluidic porous media provide an effective means of studying the flow of particles at the micrometer scale. In their work, they demonstrated the phenomenon of clogging of aqueous suspensions of uniform polystyrene spheres at the single pore level. Another work by Haw[27] used both experimental and theoretical methods to investigate the flow of concentrated suspensions of polymethylmethacrylate (PMMA) spheres through constrictions under a pressure gradient, which resulted in jamming. The findings demonstrated the jamming of concentrated suspensions in a convergent flow, leading to a phenomenon known as self-filtration. More generally, investigations at the particle scale have evidenced three main mechanisms[28] for suspensions of rigid particles, depending on the type of particle interaction and the particle-to-channel width ratio; these mechanisms are summarized in Table 1.

	Sieving	Bridging	Aggregation
Size comparison (particle diameter D, channel width W)	$D \geq W$	$D \leq W$	$D \leq W$
Solid volume fraction in suspension ϕ	Low ϕ	Large ϕ	Low ϕ
Interactions needed	Steric	Steric	Attractive particle–wall and particle–particle interactions
Clog formation	Blockage by a single particle	Blockage by an arch of particles	Successive deposition of particles leading to blockage

Table 1. Clogging in microfluidic systems: mechanisms, suspension properties, and channel geometry. Reproduced with permission from Dressaire, E., & Sauret, A. (2017), Clogging of microfluidic systems, Soft Matter, 13(1), 37-48.

The case of microgel suspensions has been much less investigated than that of colloidal suspensions. Some insights can be obtained in the case of frontal filtration of microgel particles larger than the pore size from recent works on deformable particles[29-31]. In that case, particle deformability plays a significant role (i) in the clogging of the individual pores, which can be more efficient than for rigid spheres, as the particles can partly penetrate into the pores, and (ii) in the possible compaction of the filter cake, which can lead to a decreased permeability of the cake under high pressures.

The main objective of this work is to study the jamming dynamics of an associative microgel suspension in porous media with pore sizes that are similar to or slightly larger than the particle size and to investigate the fluid loss mechanism and the filter cake buildup in such configurations. In Section 2, we present the materials studied and the various setups designed to study the phase diagram of the microgel suspensions, their rheology, and their behavior in linear channels, frontal filtration, and lateral filtration. In Section 3, we successively present the experimental results obtained with these various setups and discuss the observed phenomenology.

2. Materials and methods

2.1. Microgel preparation and characterization

The microgel suspension used in this work is an industrial microgel suspension (available at about ~ 4 wt% active in water) provided by Syensqo. It consists of loosely cross-linked amphiphilic copolymer microgel particles. Their amphiphilic character provides them with associative properties when they are dispersed in water.

The industrially-available aqueous suspension is purified by centrifugation in diluted conditions to remove all potentially large particles or aggregates from the suspension[32]. This allows for a study of filtration and flow in confined media avoiding any finite-size effects or plugging by individually large particles.

In practice, the 4 wt% microgel suspension is first diluted with water to 0.9 wt%. The 0.9 wt% suspension is then centrifuged at different speeds for 10 min using a Jouan B4 centrifuge (Thermo Scientific). After centrifugation, the supernatant is slowly extracted using a pipette. The particle size measurements in the supernatant have been performed using low-angle laser scattering with a Malvern Mastersizer 3000 granulometer. For size analysis, the microgel particles are modeled as spheres, and their refractive index is taken to be 1.5. For each sample, three consecutive runs have been performed.

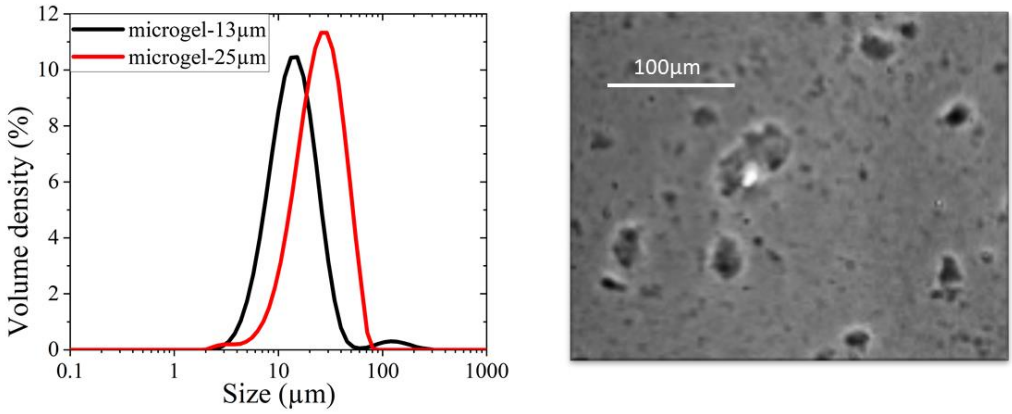

Figure 2. Left: particle size distribution of the two microgel suspensions. Right: phase-contrast image of a suspension of microgel-25µm.

Finally, two samples of monomodal distribution and moderate size dispersity have been obtained and studied (Figure 2). For a 2000 rpm centrifugation speed, the particle median diameter $d_{0.5}$ is 25 µm and the span of the distribution is 1.4; for a 4000 rpm centrifugation speed, $d_{0.5} = 13$ µm and the span is 1.9. We recall that the distribution span is defined as the normalized width of the distribution as $\text{span} = \frac{d_{0.9}-d_{0.1}}{d_{0.5}}$, where $d_{0.1}$ is the diameter below which the 10% smallest particles are found and $d_{0.9}$ is the diameter above which the 10% largest particles are found. The two studied microgels are referred to as microgel-25µm and microgel-13µm in the rest of the manuscript, in reference to their median diameter.

The microgel samples have been imaged with an Olympus IX51 microscope with phase-contrast objectives (4X and 10X). Moderate size dispersity is directly observable in the images (Figure 2). The particles appear to be somewhat elongated.

From the supernatants, suspensions at different concentrations (from 1 to 20 wt%) have been obtained by gentle evaporation in a convection oven at 50 °C for 1 to 10 days, depending on the required concentration for the experiments.

2.2. Drying for phase diagram

We have performed controlled drying experiments under a microscope to make a phase diagram of the microgel suspensions as a function of the microgel particle concentration. Confined drying provides an axial symmetry that allows a neat removal of the vapor from the droplet towards the edge of the substrate[33]. The drying kinetics can be tuned by changing the size of the substrate, as the confinement controls the evaporation process. This quasi-2D geometry allows easy observation of the drying process over time, and the average concentration $\langle c(t) \rangle$ of the suspension at any time during drying can be easily evaluated by monitoring the temporal evolution of the droplet area, $A(t)$:

$$\langle \boldsymbol{c(t)} \rangle = \frac{\boldsymbol{c_i A_0}}{\boldsymbol{A(t)}} \quad (1)$$

where c_i is the initial concentration of the suspension (at $t = 0$), A_0 is the initial area of the confined droplet (at $t = 0$) and $A(t)$ is the area of the confined droplet at any time t.

Figure 3. Schematic view of the confined cell for the drying experiment. Left: side view; right: top view.

In the drying experiments, we have used droplets of microgel suspension (volume 0.2-0.7 µl) of initial concentration $c_i = 0.7$ wt% and 1.25 wt%. These droplets are squeezed between two circular glass wafers of radii $R_w = 3.8$ cm (Figure 3). The glass wafers are spin coated with poly (dimethylsiloxane) (PDMS, Sylgard 184, Dow Chemicals) of thickness ~30 µm. This thin layer of PDMS offers a hydrophobic environment for the droplet and avoids any unnecessary line pinning and other complex phenomena for fundamental studies. In addition, PDMS can be made hydrophilic to mimic realistic surfaces. The most widely used dry method to change surface wettability is plasma surface treatment. Oxygen plasma introduces polar functional groups on the surface of PDMS, making it hydrophilic. However, it is found to

undergo hydrophobic recovery minutes after plasma treatment[34,35], which is due to reorientation of functional groups and diffusion/migration of PDMS chains from the bulk of the sample to the surface[36]. Here, to preserve the hydrophilicity of PDMS treated with plasma O_2 for a long time, we apply a surface-modifying agent provided by Syensqo[32]. The cured PDMS substrates are first treated with O_2/ air plasma for 60 s and are kept in the convection oven at 65°C for 15 min. Once at room temperature, they are put into contact with the surface modifying agent during 15 min; they are further rinsed with water before use. We have measured static water contact angles using a tensiometer (Biolin Scientific). In this work, the glass slides coated with cured PDMS are characterized by a wetting contact angle of $118°$, while the chemically treated PDMS has a wetting contact angle of the order of $4°$ and maintains its wettability for more than one day.

The distance between the glass wafers is controlled using two different PDMS spacers of thickness $h = 70$ µm and 250 µm, placed at the edge of the glass wafers. The experiments have been performed at room temperature ($T = 21$°C). External humidity is measured using a hygrometer to be in the range of 45-47%.

Images during drying have been taken using standard bright-field and phase-contrast microscopy (Olympus IX 51). For bright-field microscopy, we have used a 2X objective and for phase contrast, we have used a 4X PhC objective. The images have been collected using a CCD camera (Hamamatsu, OrcaFlash2.8). The frame rate is typically 0.1-1 fps.

Image processing has been performed to extract the droplet area, $A(t)$, as a function of time, using MATLAB®. Thresholding is used to detect the meniscus, which is comparatively darker than the rest. Bright-field images are used in this case, as they have a sharp contrast at the meniscus, and the individual particles are not seen.

2.3. Rheology

Rheological measurements have been performed with a Kinexus Ultra+ (Netzsch) stress-controlled rotational rheometer. This rheometer can be used in both stress- and strain-controlled modes (owing to torque feedback).

We have used three different geometries for rheological measurements: a smooth double-gap geometry (25 mm diameter, 1 mm gap), a sandblasted cone-and-plate geometry (40 mm diameter, $4°$ cone angle) and a sandblasted parallel-plate geometry (40 mm diameter). For the double-gap and parallel-plate geometries, the same 1 mm gap was used. The choice of

geometry is based on how concentrated and viscous the sample is. At low concentrations (low viscosity), the double-gap geometry is used, whereas the cone-and-plate geometry is used for the highest concentrations. The use of a sandblasted surface prevents slippage. The parallel-plate geometry is used for the filter cake characterization (see Section 2.2.4). The sample temperature has been kept at 25°C using a Peltier plate. Care has been taken to avoid air bubbles when loading the sample into the geometry. All experiments have been performed using a solvent trap to minimize evaporation.

The flow behavior is measured by applying increasing step values of constant shear stress and then decreasing shear stress steps. The time of the steps is adjusted to ensure that a steady state is reached. The mean shear rate and viscosity at steady state are determined for each stress value.

To study the possible aging of the suspension, the same flow measurements have been performed on semidilute suspensions at different times, ranging from 1 to 17 days after their preparation. No differences have been observed, which means that the samples are stable and free of aging over a period of more than 2 weeks.

2.4. Frontal filtration with a small pore size

We first study the filter cakes that form by accumulation on a porous material with a pore size much smaller than the particle size, that is, when the particles do not penetrate inside the porous material. We limit ourselves to frontal filtration and to the study of the cake formed at steady state under high pressure.

We use an experimental setup (Figure 4) developed by Decock and described in detail in[37]. A transparent millifluidic polycarbonate cell is used, which allows the visualization of the cake formation. The dimensions of the parallelepiped cells are: 10.2 mm in length, 2.1 mm in width, and 38 mm in height. Flow is enforced at the top of the channel through a 1.3 mm hole; the fluid exits from the cell through another hole located after the filtration elements. The bottom of the parallelepiped cell, before the exit, is covered with a Whatman nylon membrane filter of 1 µm pore size and 100 µm thickness; the cake thus forms on this membrane. We have measured the membrane permeability by measuring the pressure gradient across it at various flow rates and using Darcy's law; we have found a permeability of 1.6×10^{-14} m^2. A highly permeable mesh (Syensqo) of 460 µm thickness provides mechanical support to the membrane filter without further hindering the fluid flow. The cell input connection is

connected to a syringe (Gastight, Hamilton) with a PFA tube (internal diameter 2.4 mm). The syringe is placed on a syringe pump (Harvard PHD 4400) that controls the flow rate. An analog pressure sensor (Honeywell, range: 0-7 bar) is connected to a nanoport situated above the filter cake, which allows the monitoring of the pressure gradient across the filter cake, since the outlet of the cell is at the atmospheric pressure.

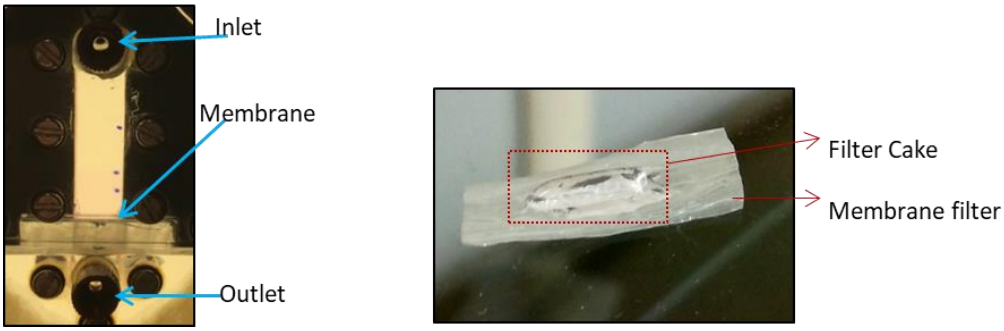

Figure 4. Left: Image of the filtration cell. Right: Image of the filter cake formed on the membrane.

To form the filter cake, we first fill the cell with a 1.8 wt% microgel suspension up to a quarter of the volume of the channel. The rest of the cell is filled with deionized water. Deionized water is then injected with a downward flow at a constant flow rate of 100 µl/h for 15 h through the channel to form the microgel filter cake on the filter membrane. This total volume of 1.5 ml (8 times the initial volume of the microgel suspension) ensures that there is enough water to push the microgel suspension onto the membrane and form a steady filter cake.

The filter cake acts as a dense porous medium, and its permeability can be calculated using Darcy's law by measuring the pressure gradient across the filter cake at various applied flow rates. To do this, we start the measurements by injecting deionized water at a constant flow rate of 100 µl/h until the pressure reaches 6-7 bar. This is done to subject the filter cake to the same pressure conditions under which it is formed. We then start to decrease the flow rate by steps, and we measure the corresponding steady-state pressures. Since the filter cake is a deformable porous medium, care is taken to work in the low-flow-rate regime so as not to excessively deform the filter cake. To measure the permeability of the cake, knowledge of its thickness is needed; it can be estimated because of the transparency of the cell.

We also characterize the rheology of the filter cake. The rheological measurements are made with a Kinexus Ultra+ rheometer (Netzsch) equipped with a sandblasted parallel-plate geometry of diameter 40 mm; the gap size is set at a low value of 100 µm due to the small amount of material extracted from the experiment. Because the volume of the filter cake recovered on the membrane is quite small, it wets only a small area of the parallel-plate

geometry. We measure the true radial dimension of the filter cake R_{real} from the observed wetted area on the plate geometry at the end of the experiment. This value is used to calculate the actual values of shear stress, shear strain, and shear rate with the standard equations of parallel plate geometries[32].

To measure the particle concentration in the filter cake, we have used an IR Moisture Analyzer (IR 60, Denver Instruments). The wet samples are placed in an aluminum pan inside the analyzer and dried at a temperature of $120°C$. Heating stops when the weight stabilizes, that is, when the solvent has evaporated. The ratio between the final mass and the initial mass then provides the solid content fraction.

2.5. Filtration with a large pore size: microfluidics

To study the mechanisms of filtration when the pore size is of the order of the particle size, we have used microfluidics with micromodels of porous materials, which allows one to design model geometries and visualize the processes at play. Here, we limit ourselves to two situations: frontal and lateral filtration over a single layer of microchannels.

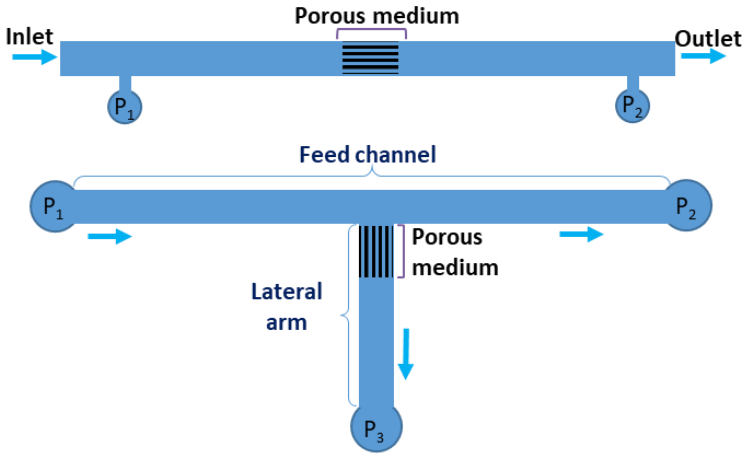

Figure 5. Top: Sketch of the channel and porous medium for frontal filtration. Here, the flow starts at the inlet and the outlet goes to the bin maintained at atmospheric pressure; the pressure probes are connected at the ends P_1 and P_2. Bottom: Sketch of the channels and porous medium for lateral filtration. The feed channel connects the ends P_1 and P_2. The lateral arm with end P_3 is joined to the feed channel via a porous array of elongated microchannels. Three different pressures are imposed to enforce the flow.

Specifically, the model designs consist of a simple straight channel of a large rectangular cross section, with either a central local restriction section comprised of model pores through which the microgel suspension is forced to flow at a constant flow rate (frontal filtration), or a lateral arm separated from the main channel by the model pores, where the flow is partly deviated

to simulate fluid loss by applying depressurization (lateral filtration) – see Figure 5. The model pores are a series of equi-spaced parallel channels of square cross section and of dimension comparable to the median particle size of the associative microgel particles (more details are provided below). Flow along a single channel of dimension similar to the model pores is also investigated.

Micromodels have been fabricated using standard soft lithography of polydimethylsiloxane (PDMS), which involves casting and curing over silicon master molds with the desired template design. The PDMS stamps and PDMS coated glass slides are oxidized in O_2 plasma and are irreversibly sealed together[38]. The Si master mold is made by conventional photolithography using a negative photoresist (SU8 3050, 3035 Microchem). More details can be found in Kaushik[32]. PDMS is hydrophobic, which is not representative of rocks that are hydrophilic; hydrophobicity may prevent microgel particles from sticking to the walls. Here, to preserve the hydrophilicity of O_2 plasma-treated PDMS, we apply a surface modifying agent provided by Syensqo (see Section 2.2.2). The surface-modifying agent is injected into the channels once they are at room temperature. After 15 min, water is flushed through the channels for rinsing. The hydrophilic microchannels are then used for experiments. We recall that we have measured a wetting contact angle of $118°$ for PDMS, while chemically treated PDMS has a wetting contact angle of the order of $4°$.

The experiments in linear channels and porous media for frontal filtration are flow-driven experiments using a syringe pump (PHD2000, Harvard Instruments), while those in porous media for lateral filtration are driven at constant pressure using a microfluidic Flow Control System (Fluigent). The differential pressure is measured along the channel for various flow rates using a pressure sensor (range 0-1 bar and 0-7 bar, ASDX series, Honeywell) connected to an Arduino data acquisition card, while the flow rates are measured using a high-precision flow sensor (Fluigent).

All microfluidic experiments presented here are conducted at room temperature (21 ± 2°C). We have used video phase-contrast microscopy to record the images of the porous channels and observe the jamming dynamics of the microgel suspension. The optical setup consists of an inverted microscope (IX 51, Olympus) equipped with a CCD camera (Hamamatsu, OrcaFlash2.8). We have also used fluorescence microscopy. For fluorescence visualization, the suspensions were seeded with fluorescent tracer particles (Fluosphere, Carboxylate 1 µm, Life technologies). Exposure times varied according to the flow rates used in the experiments.

2.5.1. Single linear channels

We have used linear microfluidic channels of total length $L_T = 2$ cm with a distance $L = 1$ cm between the pressure probes, while the channels are designed with different heights (H) and widths (W) (see Table 2). These dimensions are chosen to be close to those of the pores used in the filtration experiment and to investigate possible changes in the behavior and jamming due to finite-size effects.

	Width W	Height H
Channel A	20 µm	15 µm
Channel B	45 µm	30 µm
Channel C	85 µm	60 µm

Table 2. Dimensions of linear microchannels A, B, and C.

We have used 0.4 wt% microgel-25µm in these experiments. This semidilute suspension has Newtonian behavior, and its viscosity is 2.4 mPa s (see Section 3.3.2). We recall that the median particle size is 25 µm for this microgel. Channel A is thus slightly smaller than the particle size, meaning that the particles are deformed in this channel and are likely to be advected one by one. Channel B is only slightly larger than the particle size, and channel C is a couple of particles wide and high.

Using the standard equations for flow in a rectangular channel to extract the wall shear stress and the wall shear rate from the imposed flow rate and the measured differential pressure[32], it is possible to plot the local flow curve and compare it with the flow curve measured with the rheometer.

2.5.2. Porous media – Frontal filtration

The model porous medium for frontal filtration consists of an array of microchannels of length $L = 200$ µm (Figure 6). These microchannels are placed parallel to the flow direction in the middle of the main channel. We varied their width (w_p) and height (h) and the gap (w_g) between them (see Table 3).

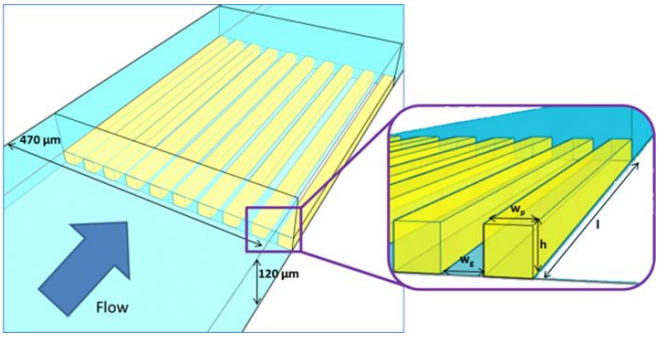

Figure 6. Sketch of the model porous medium for frontal filtration.

Width of the microchannels, w_p (µm)	Gap between microchannels, w_g (µm)	Height of the microchannels, h (µm)	Name given
20	20	20	Frontal-20
40	40	40	Frontal-40

Table 3. Dimensions of the microchannels that form the porous medium and names given to the channels used for the flow experiments.

Before and after the porous array, the main channel dimensions are: 120 µm height and 470 µm width, which makes the overall channel stepped. This is done to avoid any self-filtration before the suspension reaches the porous part. All experiments are carried out at room temperature (21°C).

The pressure probes are connected at P_1 and P_2 and the flow is induced at the inlet (Figure 5). The outlet is connected to a bin that is kept at atmospheric pressure.

Running a preliminary calibration with water flow at various rates, the permeability of the porous section has been determined using Darcy's law[32]. It is 1.5×10^{-12} m^2 for the model porous section with 20 µm x 20 µm channels.

2.5.3. Porous media – Lateral filtration

The porous channels for lateral filtration are T-shaped channels with the porous part located at the junction of two arms (Figure 7). One arm constitutes the main input channel of 470 µm width and 180 µm height, connected to the ends P_1 and P_2 (Figure 5). As in the frontal filtration experiments, the porous part is made up of an array of microchannels that lie perpendicular to the feed channel. The microchannels are followed by a lateral arm of 470 µm width and 180 µm height that leads to an outlet P_3 (Figure 5). The dimensions of the microchannels are length $L = 200$ µm, height $h = 20$ µm, width $w_p = 20$ µm, and the gap between them is $w_g = 20$ µm. This setup is named Lateral-20 in the rest of the paper.

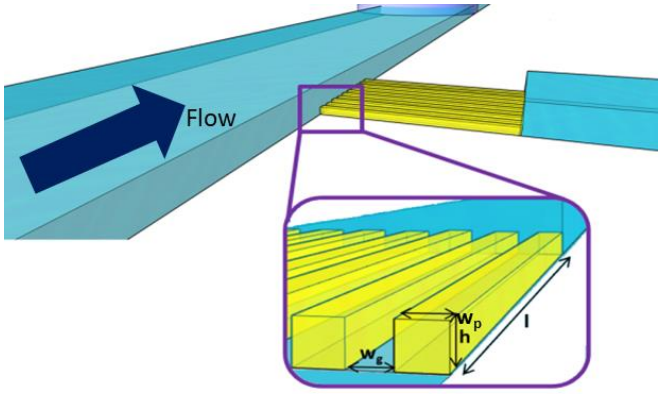

Figure 7. Sketch of the porous medium for lateral filtration.

During experiments, the flow rate is measured as a function of time in the lateral arm. The flow sensor is connected to the end P_3 with the help of a long PFA tubing (~ 1 m) with a water buffer column to avoid contamination of the flow sensor due to the microgel suspension. The experiments have been carried out with a 0.8 wt% microgel-25µm.

P_1 (mbar)	P_2 (mbar)	P_3 (mbar)
40	20	10
60	30	15
80	40	20
100	10	1

Table 4. Pressure maintained at the ends P_1, P_2, and P_3 in porous media for lateral filtration.

The experiments carried out in porous channels for lateral filtration are pressure-controlled experiments with constant air pressure ($P_1 > P_2 > P_3$) applied at the three ends (Figure 5). The goal of using pressure control is to simulate fluid loss in the rock and to see if the flow to the porous material can be stopped owing to the microgel. We used pressurized air to control the pressure applied to the microgel suspension. The pressure values used in the experiments are mentioned in Table 4.

3. Experimental Results

In our experiments, a filter cake is expected to be a concentrated microgel suspension with a yield stress. Before investigating filtration, it is therefore important to have an idea of the phase diagram of the suspension as a function of the microgel particle concentration; this is the focus of Section 3.3.1. The rheology of the suspensions is then studied for various particle fractions (Section 3.3.2). Filtration is finally investigated in Sections 3.3.3 and 3.3.4.

3.1. Phase diagram

Drying experiments (Section 2.2.2) are performed with hydrophobic PDMS; this ensures the most homogeneous drying possible, without loss on the surface during the process (Supplementary Material, Appendix A). We use two different initial concentrations, $c_i = 0.7$ wt% and 1.2 wt%, of microgel-25µm and microgel-13µm. The gap is fixed either to 70 µm or to 250 µm. Bright-field snapshots of the drying of a microgel suspension in the confined cell are shown in Figure 8.

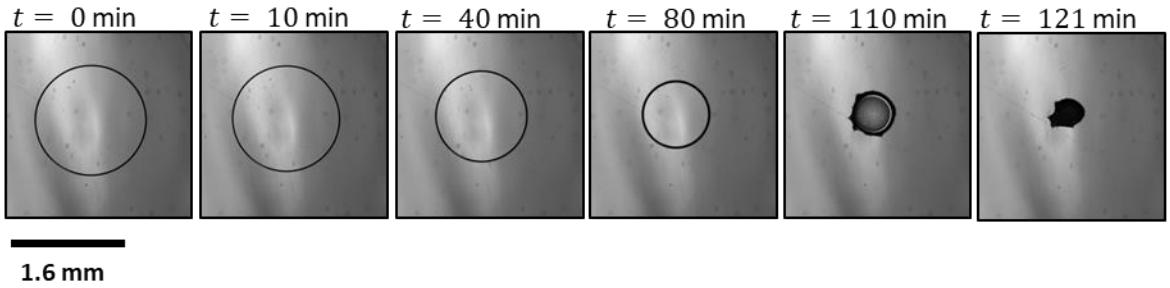

Figure 8. Series of bright field images during the confined drying of a droplet (~µl) of microgel-13µm of initial concentration $\boldsymbol{c_i} = \mathbf{1.2}$ wt% squeezed between two hydrophobic circular wafers with a $\mathbf{70}$ µm gap.

It is observed that the droplet retains a cylindrical geometry during the first stage of drying, while it shrinks as the solvent evaporates from the droplet edges. At some point (time $t = 110$ min in Figure 8), the droplet is no longer perfectly circular, due to pinning of the meniscus; drying then continues by deforming the droplet interface. Another interesting effect, which begins simultaneously with the pinning of the meniscus, is the decrease of the light intensity within the drop, which continues until the end of drying. As the surfaces are hydrophobic, the pinning of the interface can be attributed here to the jamming of the suspension and the emergence of a yield stress, as classically observed in the drying of suspensions[39,40]. The interface then resists deformation, which explains its noncircular shape: the mechanical properties are not perfectly homogeneous and droplet deformation occurs at the weakest point. The drop in light intensity corresponds to cracks and air intrusion in the droplet. Here, the droplet continues to shrink for a long time due to particle deformation; as the drying continues, the capillary stresses are higher and higher, and the droplet shrinking is expected to stop only when the particles are fully packed, at a particle volume fraction close to 100%. As we will see in Section 3.3.3, the final particle fraction reached here is consistent with the particle fraction reached under frontal filtration on small pores at high pressure. This explains why shrinkage in the jamming regime is much more important here than with hard spheres[41]. The particle concentration in the droplet during drying is shown in Figure 9. It is observed that the concentration saturates at a value c_m of order 12 wt%, which likely corresponds to the maximum volume fraction achievable with these deformable particles, that is, 100%. Note that c_m is only roughly estimated in these experiments as the final droplet shape is rather complex; another estimate is provided in Section 3.3.3.

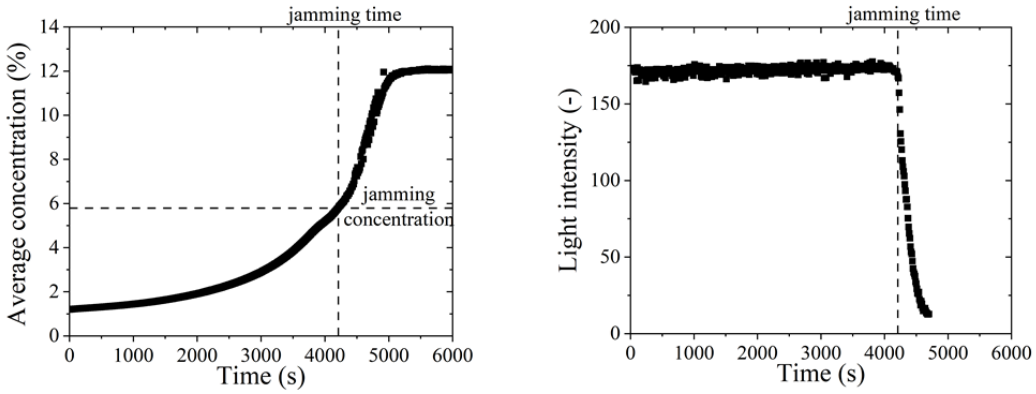

Figure 9. Temporal evolution of the average concentration and of the light intensity (arbitrary units) in a drop of microgel-13µm of initial concentration $\boldsymbol{c_i = 1.34}$ wt% confined in a circular cell of $\mathbf{70}$ µm gap.

We also plot the temporal evolution of the change in intensity in a small region of interest in the middle of the droplet. We see that the intensity before 4210 s remains constant in time. After $t_j = 4210$ s, a sudden drop in intensity is observed. As discussed above, t_j corresponds to the time at which the jamming concentration is reached inside the droplet. We can then determine the jamming concentration c_j from the average concentration versus time plot. We find $c_j = 6.8$ wt% for both microgel-25µm and microgel-13µm. As we will see in Section 3.3.2, this value of c_j is in fair agreement with the value obtained for the emergence of a yield stress in the bulk rheology. Now we try to estimate roughly the jamming volume fraction of the microgel-13µm and microgel-25µm using these results. Typically, ϕ_m represents the maximum packing fraction when the particles are closely packed. In ideal situations, for deformable but incompressible particles, $\phi_m = 1$. This ϕ_m corresponds to the concentration c_m observed at the end of drying. The jamming concentration c_j corresponds to the jamming fraction ϕ_j. For non-frictional monodisperse hard spheres, $\phi_j = 0.64$; for frictional spheres, it depends on the interparticle friction coefficient and can be as low as 0.55[42]. For our particles, we can try to estimate ϕ_j as

$$\frac{\boldsymbol{\phi_j}}{\boldsymbol{\phi_m}} = \frac{\boldsymbol{c_j}}{\boldsymbol{c_m}} \tag{2}$$

Using this equation and the measurements made in the drying experiments, we finally estimate ϕ_j to be of order 0.56 for both microgel-13µm and microgel-25µm, which is close to the value one gets for frictional hard spheres. This finally leads to the schematic phase diagram presented in Figure 10, which will be supplemented by the characterization of the rheological behavior in the next section.

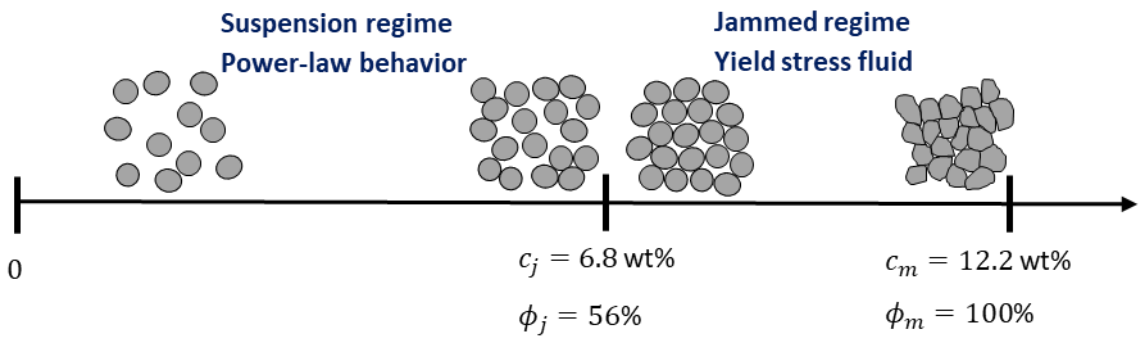

Figure 10. Phase diagram.

We have performed other drying experiments to obtain an estimate of the jamming concentration by varying the initial concentration and the gap between the glass wafers. For a 70 µm gap, for 0.7 wt% of microgel-13µm and of microgel-25µm, we find $c_j = 6.6$ wt%. For an initial concentration of 1.2 wt% and a 250 µm gap, we find $c_j = 6.3$ wt% for both microgel-25µm and microgel-13µm. Clearly, the jamming concentration seems to be affected only marginally by the initial concentration of the suspension and the confinement. This turns out to be a rather important result when considering the flow of suspensions in micrometer-sized channels and porous media.

3.2. Flow behavior

In this section, we study the steady-flow behavior of the suspensions of microgel-13µm and microgel-25µm under imposed shear stress steps. The flow curves of the microgel-13µm are shown in Figure 11.

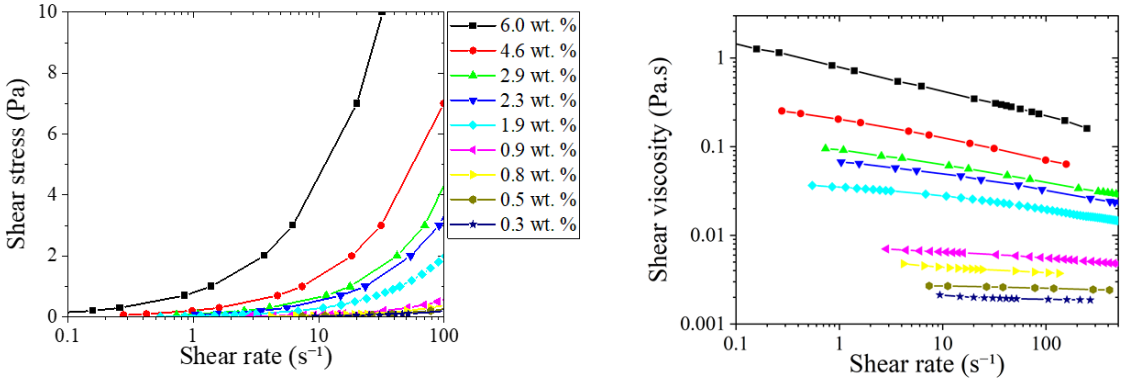

Figure 11. Steady flow curves for concentrations ranging from $\mathbf{0.3}$ wt% to $\mathbf{6.0}$ wt% for microgel-13µm. Left: shear stress versus shear rate; right: shear viscosity versus shear rate.

The suspensions exhibit shear-thinning behavior. As the concentration c increases, the shear thinning becomes more pronounced. Above a jamming concentration c_j between 6 and

6.8 wt%, a yield stress is observed. However, the microgel suspensions formed beyond c_j are inhomogenous and lumpy (controlled materials might be obtained by osmotic confinement instead of drying); this leads to poor reproducibility, which is why we did not investigate this regime in detail.

The flow curves are well described by a power law model $\sigma = k\dot{\gamma}^n$ for $c < c_j$. The power law index n obtained from a fit of the data to a power-law model are shown in Figure 12. It is observed to decrease regularly with the particle volume fraction, down to $\simeq 0.65$ close to the jamming concentration c_j. This is consistent with previous observations and theories for suspensions of deformable particles; e.g., an exponent $n = 0.66$ is predicted and observed in concentrated emulsions close to c_j[43]. Shear thinning is mostly due to the interplay between shear and deformability. Note that varying friction might also play a role in shear thinning for deformable particles as for hard particles[44,45].

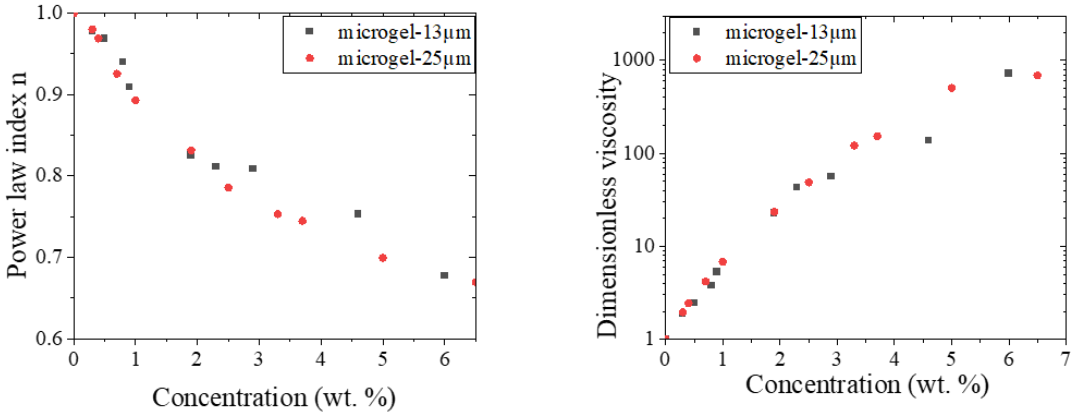

Figure 12. Left: Power-law index $\boldsymbol{n}$ as a function of concentration c. Right: dimensionless viscosity (measured at **1** Pa shear stress) as a function of concentration (wt%). Plots for both microgel-13µm and microgel-25µm.

We also plot in Figure 12 the dimensionless viscosity η as a function of the concentration c for the microgels, where $\eta = \frac{\eta_s}{\eta_f}$, with η_s the suspension viscosity and η_f the suspending fluid viscosity (here, water). Because suspensions are shear thinning, the viscosity has to be estimated at a given shear stress or shear rate. Since the deformability and frictional properties of sheared suspensions are controlled by the interparticle force, which is proportional to the shear stress with a proportionality factor that is only slightly dependent on the particle concentration[46], it seems relevant to evaluate η_s at the same shear stress for all particle concentrations in order to compare similar states. Here, we plot the dimensionless viscosity as evaluated for a shear stress of 1 Pa.

The viscosity increases regularly with concentration, with an approximately exponential increase up to a given jamming fraction c_j of order 6.5 to 6.8 wt%, consistent with the value observed in the drying experiment. In contrast to suspensions of rigid particles, no clear divergence of the viscosity is observed, which might be attributed to the softness of the particles.

At concentrations beyond c_j, we have only qualitatively studied the behavior of the obtained yield stress materials. The yield stress σ_y has been estimated as the stress below which no steady flow is observed. A yield stress of the order of 0.5 Pa has been found for 6.8 wt% microgel-13µm and a yield stress of the order of 5 Pa has been found for a 8.5 wt% microgel-25µm. Given the observations made in the confined drying experiments, materials with a higher yield stress can be expected to form as the particle concentration increases. We will return to this point in the next section, where a high-concentration filter cake will be formed and characterized.

The phase diagram of Figure 10 is finally completed with reference to the observations made on the rheological behavior. For $0 < c < c_j \simeq 6.8$ wt% corresponding to $0 < \phi < \phi_j \simeq 56\%$, the material is a liquid microgel suspension with a power-law behavior, whereas for $c_j < c < c_m \simeq 12.2$ wt% corresponding to $\phi_j < \phi < \phi_m = 100\%$, it is a jammed microgel suspension, with a yield stress fluid behavior.

3.3. Frontal filtration with a small pore size

The simplest filter cakes that can be formed are those formed by frontal filtration on a porous material with a pore size much smaller than the particle size. In such a situation, the particles simply accumulate on the surface of the porous material to form a filter cake, the permeability of which depends on the (local) particle concentration. Here, we are interested in forming the most efficient filter cake, as concentrated as possible (that is, of volume fraction close to 100%), in order to have an order of magnitude estimate of the lowest cake permeability achievable with such particles. The filter cake is formed as described in Section 2.2.4.

Permeability

The steady-state pressure drop values ΔP are displayed in Figure 13 for both the microgel-13µm and microgel-25µm as a function of the applied flow rate Q. We observe a linear increase of ΔP with Q up to $\sim$ 3-4 bar. Above this value, the ΔP vs. Q slope decreases. This departure from a linear regime is likely due to the deformation of the microgel filter cake

because of the high-pressure gradient. This deformation might fracture the filter cake and form preferential paths that allow the fluid to pass more easily through the filter cake.

The permeability $\mathcal{K}$ is calculated using Darcy's equation in the linear regime as

$$\boldsymbol{\mathcal{K}} = \frac{\boldsymbol{\eta}\, \boldsymbol{L}}{\boldsymbol{A}*(\frac{\boldsymbol{\Delta P}}{\boldsymbol{Q}})} \tag{3}$$

where A is the cross-section area of the filter cake and η is the viscosity of the fluid (here, water). The height L of the cake, of order mm, is hard to determine accurately from visual observation. To estimate its value, we simply weigh the filter cake at the end of the experiment; by using c_0, L_0, and m_0 as the initial concentration, microgel suspension height, and mass of microgel suspension injected in the cell, and m_f the mass of the filter cake formed in the cell, we can estimate the thickness of the filter cake L as $L = \frac{L_0 * m_f}{m_0}$ when the density of the microgel is close to that of the suspending fluid.

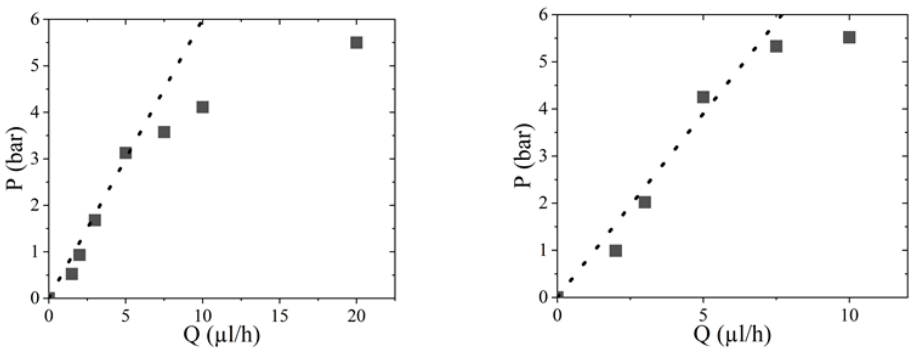

Figure 13. Pressure $\boldsymbol{P}$ versus flow rate $\boldsymbol{Q}$ plot for filter cake of microgel-13µm (left) and microgel-25µm (right). The dotted lines are guides for the eye.

Finally, we estimate that the permeability of the filter cake is of the order of 3×10^{-19} m^2 for both the microgel-13µm and the microgel-25µm. Such low permeability is often observed in rocks such as granite, which has permeability values typically between 10^{-19} and 10^{-22} m^2, implying the very impervious nature of the filter cake to the flow of water.

Concentration

To measure the concentration of the filter cake, we perform dry mass measurements. After the permeability measurements are made, the cell is opened and the filter membrane with the filter cake stuck to it is carefully removed. The microgel filter cake is scraped off the membrane using a spatula. The filter cake is then dried at high temperature inside an infrared moisture analyzer. The estimated final concentration (c_f) is similar for the two microgel suspensions and is found to be 12.2 wt%, This concentration of the filter cake can be seen as

the concentration for the maximum packing of the microgel particles (i.e. a particle volume fraction of $\sim 100\,\%$); it is consistent with the value observed at the end of the drying experiment of Section 3.3.1.

Porosity

Now, we try to evaluate the porosity ϕ_p of the filter cakes from the observed value of the permeability. ϕ_p is the volume fraction of the voids in the porous system related simply to the particle volume fraction ϕ by $\phi = 1 - \phi_p$.

Many semi-empirical laws have been proposed to describe the permeability $\mathcal{K}$ as a function of the pore size λ_p (typically, the spacing between the particles in the filter cake) and of ϕ_p. The most used equation is the relation of Carman-Kozeny:

$$\boldsymbol{\mathcal{K} \simeq \lambda_p^2 {\phi_p}^3} \qquad (4)$$

It has proved to be very efficient in modeling the permeability of loose particle assemblies as well as that of very dry foams[47]. For very dense packings, the main difficulty is to estimate the relevant pore size λ_p. Here, we use the equation validated by Rouyer *et al.*[47] for dry foams, which we assume to have a geometry similar to that of the densely packed deformed microgel particles:

$$\boldsymbol{\mathcal{K} = \frac{{\phi_p}^2 d^2}{1248\left(1-2.15\phi_p+1.37\phi_p^2\right)^2}} \qquad (5)$$

where d is the bubble diameter in [47] and is here the microgel particle diameter. Note that in this framework, the $\boldsymbol{\mathcal{K}}$ values for the filter cakes formed with the microgel-13µm and the microgel-25µm should have differed by a factor 4 if they had had the same structure; this is not the case, which means that our protocol does not ensure the exact same conditions for different particle sizes.

In the limit of low porosity, with $\mathcal{K} \simeq 3 \times 10^{-19}$ m^2 we finally find $\phi_p d \simeq 2 \times 10^{-8}$ m. It suggests that the porosity ϕ_p of the filter cakes formed in our frontal filtration experiments with small pores is of the order of 0.1%, consistent with our guess that $\phi_m \simeq 100\%$.

Rheology

We measure the flow behavior of the microgel filter cake by applying a logarithmic shear-rate ramp from 0.001 to 10 s^{-1}. We recall that the raw data are corrected by taking into account the true area of the parallel plate wetted by the filter cake (Section 2.2.3). Yield stress behavior

is observed for both microgel-13µm and microgel-25µm filter cakes. From the flow curve, the yield stress, σ_y, is found to be of order 10 Pa and 5 Pa for the microgel-13µm and the microgel-25µm, respectively. This points to a $\propto 1/r_p$ dependence of σ_y on the particle radius r_p as classically found in microgel suspensions[48].

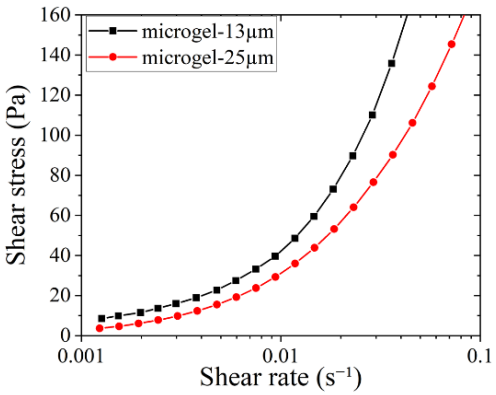

Figure 14. Flow curves of the filter cakes obtained from filtration experiments.

3.4. Filtration with a large pore size: microfluidic experiments

Now we investigate frontal and lateral filtration in microchannels. We focus on the case of semidilute suspensions at concentrations lower than 1 wt% (corresponding to a particle volume fraction less than 10%).

3.4.1. Single linear channels

We first look at flows in linear channels of size similar to that of the microchannels composing the model porous materials in the filtration experiments (Table 2). The flow curves extracted from the steady pressure drop ΔP vs. flow rate Q measurements for a 0.4 wt% microgel-25µm in channels of size slightly larger than the particle median diameter are shown in Figure 15. The same behavior is observed in the channels as in the rheology experiments, although at much higher shear rates, that is, a Newtonian behavior with a viscosity of 2.8 mPa in channel B and 2.3 mPa.s in channel C, to be compared to the value of 2.4 mPa measured with the rheometer.

For experiments in a channel slightly smaller than the median particle diameter (channel A), due to the high pressure involved, it was possible to perform experiments at only a very low flow rate, corresponding to $\sim 10\,000$ s^{-1} shear rate. In that case, finite-size effects and wall friction of the deformed particles lead to a moderately higher viscosity of 8.7 mPa.s; it is worth noting, however, that no jamming is observed and that the behavior remains purely viscous with a rather low viscosity.

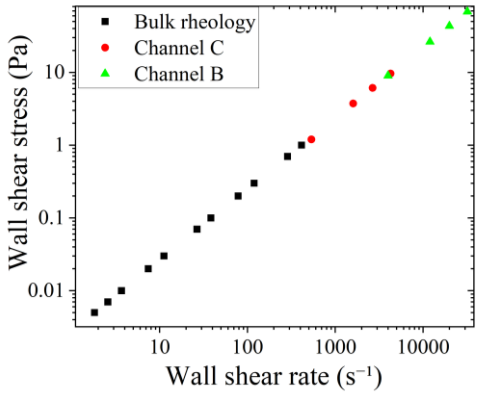

Figure 15. Plot of wall stress (Pa) versus wall shear rate (1/s), calculated using the working equations for flow in a rectangular channel in channels B and C, and of shear stress versus shear rate obtained from rheological measurements, for $\mathbf{0.4}$ wt% microgel-25µm.

It can be concluded that, in the microchannels that constitute the model porous materials in the frontal and lateral filtration experiments that will be discussed in the following, no jamming, and thus no cake formation would be expected in principle.

3.4.2. Frontal filtration

We now investigate frontal filtration of semi-dilute microgel suspensions. Here we discuss in detail the behavior observed with a 0.8 wt% (~ 7% volume fraction) microgel-25µm driven at a constant flow rate through the Frontal-20 porous channel. The same phenomenology has been observed with more dilute suspensions and with slightly larger pore-to-particle size ratios (this is briefly discussed in the Supplementary Material, Appendix B**Erreur ! Source du renvoi introuvable.**).

We first consider flows at a constant flow rate $Q = 100$ µl/h. Under these conditions, the average velocity in the main channel is of the order of 0.5 mm/s and the typical shear rate is of the order 4 s^{-1}; in the microchannels, the average velocity is of the order of 5 mm/s and the typical shear rate is 3500 s^{-1}, which corresponds to the regime investigated in the single linear channel experiments. Assuming that the velocity varies over typically 100 µm from the main channel to the microchannels, the associated extensional shear rate is of the order of 5 s^{-1}.

Figure 16 shows a series of phase-contrast micrographs (the full movie is shown in the Supplementary Material), and Figure 17 shows the simultaneous evolution of the pressure drop in time. Here, we define time $t = 0$ s as the time when the first particle is observed to reach the array of microchannels.

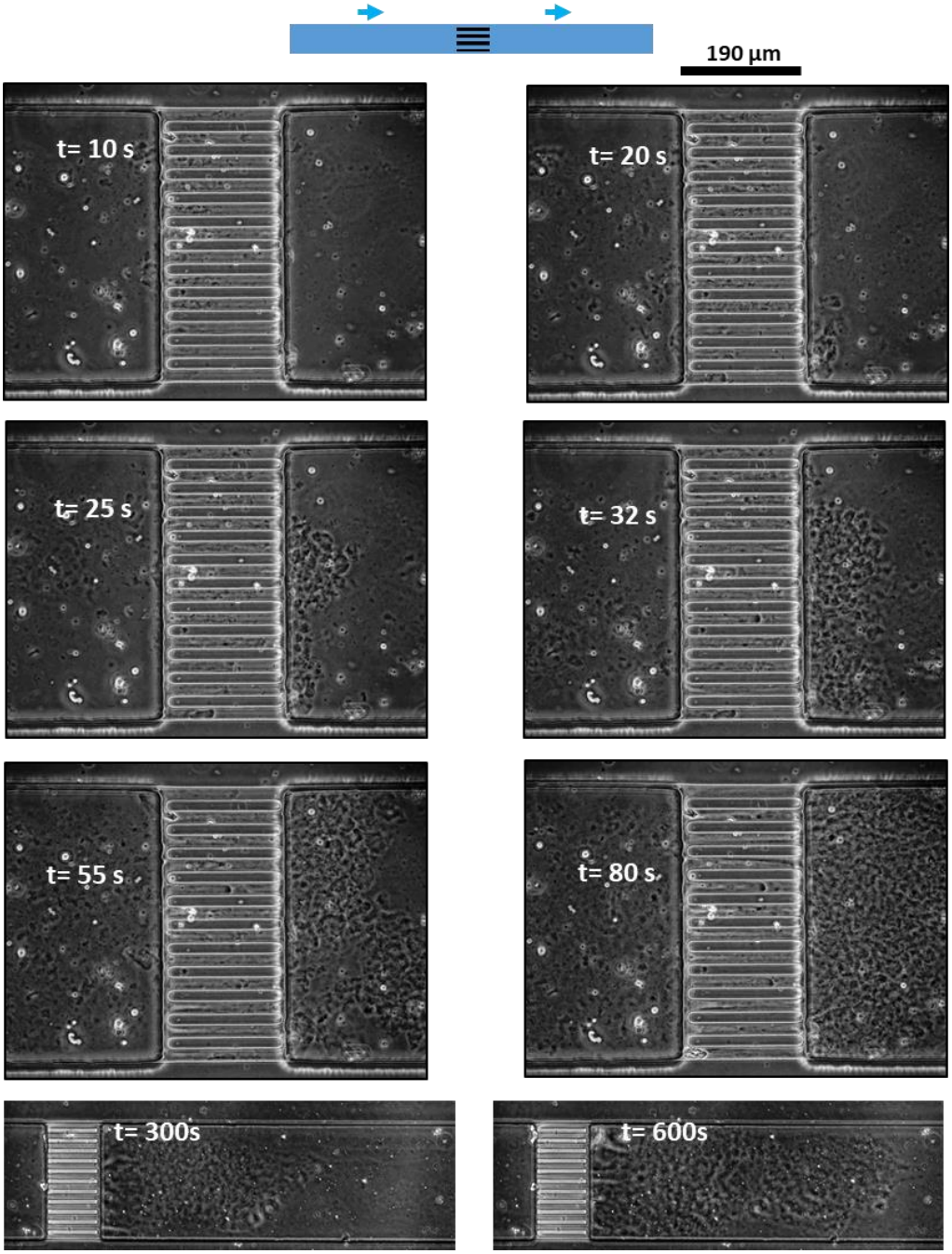

Figure 16. Phase contrast snapshots (with a 10X objective) showing the jamming dynamics in frontal filtration of 0.8 wt% microgel-25µm at a constant flow rate *Q*= 100 µl/h in the Frontal-20 porous channel. The 2 images in the last row are taken with a 4X objective in a replicated experiment under the same conditions**.**

It is observed that as the particles pass through the porous array, they start to aggregate in the microchannels. When the microchannels are jammed, the particles continue to aggregate in the downstream channel, at the exit of the microchannels (time $t = 20$ s). A solid-like jammed material forms that eventually covers the entire porous material at its exit with a layer of particles forming a first shallow cake (time $t = 32$ s). As the flow continues, the aggregation process continues, still at the exit of the porous material: the aggregate grows in

the downstream channel and eventually invades the whole channel after a very long time. The growth rate of the filter cake appears to be constant, suggesting simple accumulation at the exit of the porous material, since the flow rate is imposed in these experiments.

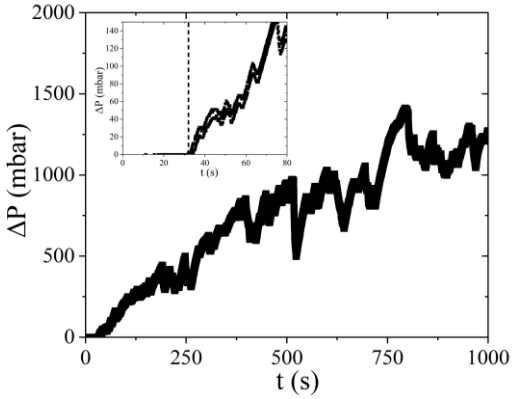

Figure 17. Pressure drop across the Frontal-20 channel for the flow of $\mathbf{0.8}$ wt% microgel-25µm at a constant flow rate $\boldsymbol{Q} = \mathbf{100}$ µl/h. The inset is a zoom in on the first $\mathbf{80}$ s; the dotted line shows the jamming time.

In parallel, the pressure, initially constant and low, consistent with the Newtonian behavior of the semi-dilute microgel suspension and its low initial viscosity, begins to grow significantly when the first layer of jammed material covers the entire porous material at its exit ($t \simeq 32$ s). Then it increases roughly linearly over time, consistent with the linear growth in time of the filter cake and with Darcy's law; the corresponding permeability of the filter cake can then be estimated as being of order 5×10^{-15} m^2 (this is discussed in more detail below). We also observe large fluctuations of the pressure, in the form of sudden drops during short periods. These drops correspond to transient fractures in the jammed material (seen in the movie), which form preferential paths for water.

It is obvious from the movie shown in the Supplementary Material that, although the microchannels are jammed with an aggregated microgel, no aggregation occurs in the upstream channel: there is no filter cake at the entrance of the porous section. In the jammed state, from time to time, the particles arriving at the entrance of the porous section abruptly penetrate into one of the microchannels of the porous section, which eventually partially extrudes the jammed material from the microchannel to the downstream channel, eventually leading to the growth of the filter cake.

It is also observed in the movie that the filter cake is slowly eroded, since particles from the first layers of the filter cake in the downstream channel tend to be detached and convected in the channel. Some particles are also likely to be transported when transient fractures form (see above). The growth rate of the filter cake then results from the complex interplay of

aggregation in the microchannels and of the filter cake. Here, we estimate that 10 % of the particles are trapped in the filter cake.

We checked that the microgel jams along the entire height of the downstream channel thanks to an experiment performed with a 0.8 wt% microgel-25µm seeded with fluorescent tracers. Using fluorescence microscopy, we have indeed observed that there are motionless tracers at the same concentration in all focal planes from $z = 0$ to 120 µm in the downstream channel[32].

Discussion.

The most striking feature of this model filtration test is that the filter cake is formed on the downstream side of the porous section. In a standard filtration process, one would expect that the gel particles would be either sufficiently small to flow through the channels or large enough to individually clog the channels and thus build a filter cake on the upstream side. Here, the particles are small enough (and deformable enough) to flow through the pores, and no clogging is observed in the linear microchannel flows under the same conditions (Section 3.3.4.3.4.1), yet full pore volume jamming is observed as well as jamming in a significant section of the downstream channel after sufficiently long filtration times.

This phenomenon is most likely related to shear-induced aggregation, as described in the literature, when the shear applied to a particle suspension is high enough for the hydrodynamic force to overcome the stabilizing repulsive interactions[49]. For example, Wu et al.[50], studying the jamming of particles in a microchannel bottle neck with a colloidal dispersion noticed that, below a critical shear rate, the jamming rate is slow, as the hydrodynamic forces are not high enough to overcome the repulsive potential barrier. Above this critical value, aggregates are formed, although sometimes breakage of the aggregates can occur[51]. However, since shear-induced aggregation does not occur in linear microchannel flows under the same conditions, rather than being induced by high shear rates in simple shear flows, it seems here that the aggregation is induced by the extensional flow due to the contraction/extension from the upstream channel to the porous section; we recall that the extensional shear rate is estimated here to be of order $5\ \mathrm{s}^{-1}$. This extensional-shear-induced aggregation process would allow individual associative microgel particles to interconnect and aggregate, finally forming a solid-like sticky gel filling the microchannels and the downstream section. The possible importance of extensional flow is reminiscent of recent observations on the aggregation of proteins[52]: extensional flows have been shown to be key in promoting

aggregation, as they tend to unfold the polymers, allowing possibly attractive blocks to be brought into contact. The same might happen here with the dangling amphiphilic copolymer chains of the microgel particles: by unfolding these chains, the extensional flows might favor the association between hydrophobic groups of chains belonging to different particles. An interesting feature of these aggregates formed under extensional shear is that they are not reversible once flow stops; large gel objects remain within the filter structure and retain their ability to seal the porous section permanently.

Effect of flow rate.

We now investigate the impact of flow rate on jamming. In all cases (see Supplementary Material, Appendix B), the same phenomenology is observed. To compare the situations, we define the jamming time t_j as the time between the first particles reaching the porous section and the full jamming of the porous section (as indicated by the sudden initial rise in the differential pressure). From this jamming time, the jamming volume V_j (e.g. the volume of suspension that has flowed through the porous section prior to jamming) is calculated as $V_j = Q \times t_j$. This is plotted in Figure 18.

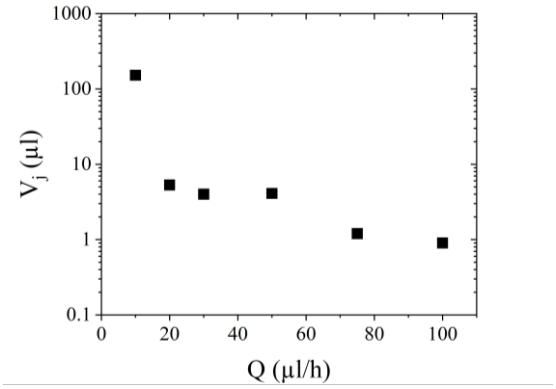

Figure 18. Jamming volume, V_j as a function of flow rate $\boldsymbol{Q}$ for $\mathbf{0.8}$ wt% microgel-25µm through Frontal-20 porous channel.

It can be seen that the jamming volume drops dramatically as the flow rate increases. It is consistent with hydrodynamically-driven aggregation. Indeed, if conventional clogging was occurring, arising from individual particles plugging the channels, one would expect the jamming volume to be almost independent of the flow rate, as this would be a purely statistical process. Here it seems that a minimal critical flow rate of about 20 µl/h is needed to trigger jamming. For this flow rate, the extensional shear rate is of the order of 1 s^{-1}. Below this threshold, individual associative microgel particles do not associate and likely take much

longer to clog the channels. At higher flow rates, the shear and drag forces are high enough to force the associative microgels into contact and induce aggregation, thus clogging the microchannels.

Permeability measurements.

Finally, we characterize the permeability of the microgel filter cakes formed within the Frontal-20 channel as a result of jamming of 0.8 wt% of microgel-25µm at a flow rate $Q = 100$ µl/h. To do that, after the cake is formed, we reverse the flow direction using only pure water and measure the pressure drop ΔP over the filter cake, which is now compressed onto the porous section. ΔP is plotted versus water flow rate in Figure 19.

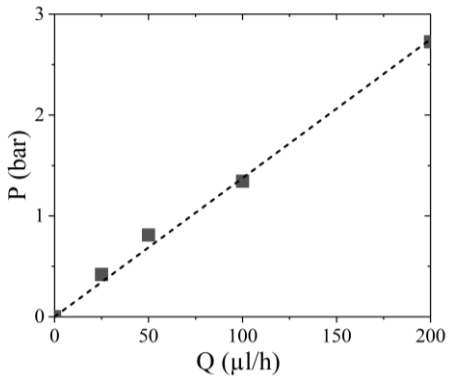

Figure 19. Frontal-20 porous channel with a $\mathbf{1}$ mm thick microgel filter cake formed at a constant flow rate of $\mathbf{100}$ µl/h : plot of pressure drop as a function of flow rate.

Linear behavior is observed, showing that the cake deformation is limited at these applied pressures. The permeability of the filter cake calculated with Darcy's law is 3.8×10^{-15} m^2. This permeability value is considerably higher than that obtained in frontal filtration with small pores, because the formation of the filter cake occurs after the porous section, in contrast to the permeability experiments, where the filter cake formed on the supporting membrane is relatively dense, because of the high compression experienced during its formation. Using Equation 5, we can estimate the particle volume fraction of the filter cake to be about 90 to 95 %, which is a reasonable value. Consistently, it belongs to the jammed yield stress fluid regime of the phase diagram of Figure 10.

3.4.3. Lateral filtration

We have shown the ability of semi-dilute microgel-25µm to form a filter cake when flowed through a porous array in the case of frontal filtration even with rather large pores. To be useful in applications such as those encountered in oil fields, a typical fluid loss additive should

also be able to form a thin filter cake on a porous material in the direction perpendicular to the direction of the main flow.

Here, we investigate the formation of a filter cake by 0.8 wt% microgel-25µm in microfluidic porous media for lateral filtration as presented in Section 2.2.5.2.5.3. The pressure at the inlet of the main channel is 40 mbar, the pressure at its outlet is 20 mbar, while it is 10 mbar in the lateral arm to simulate fluid loss. Phase-contrast images of the lateral arm and flow-rate measurements are shown in Figure 20 and Figure 21. The full movie is available in the Supplementary Material.

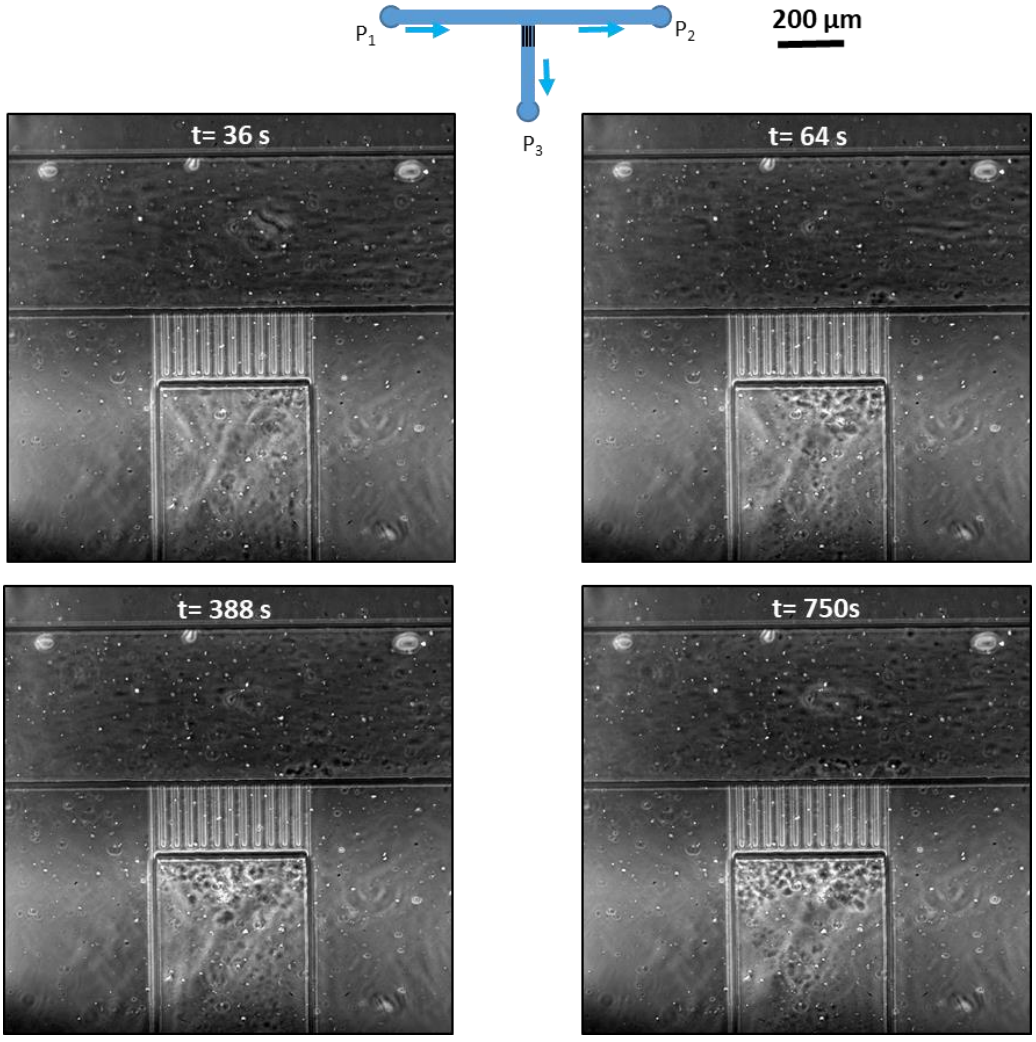

Figure 20. Series of phase-contrast snapshots over a course of time in a porous channel (Lateral-20). Pressure-driven experiment with $\boldsymbol{P_1 = 40}$ mbar, $\boldsymbol{P_2 = 20}$ mbar, and $\boldsymbol{P_3 = 10}$ mbar.

As in frontal filtration experiments, a cake is found to form inside the microchannels and to grow at the exit of the porous material that covers the lateral arm. Meanwhile, the water flow rate decreases as the cake forms. More precisely, the flow rate initially has a high steady value of 250 µl/h. It starts to decrease at time $t = 36$ s as an aggregate begins to form at the exit of

the microchannels. For some reason, this aggregate then covers only half of the porous array of microchannels for a long time, from $t = 64$ s to $t = 388$ s; meanwhile, the flow rate remains constant at a value of around 100 µl/h. The aggregate continues to grow and eventually covers the entire porous material and plugs the lateral channel at time $t = 388$ s. This is accompanied by a dramatic drop in flow rate, which then remains constant at a very low value of 2.4 µl/h until the end of the experiment. The cake formed in the lateral arm does not grow further because the microgel particles now remain in the main channel: the formed cake is sufficient to prevent efficiently fluid loss.

For the final reduced flow rate, using Darcy's law, the permeability of the filter cake is estimated to be on the order of 10^{-15} m^2, which is similar to that estimated in frontal flow filtration experiments.

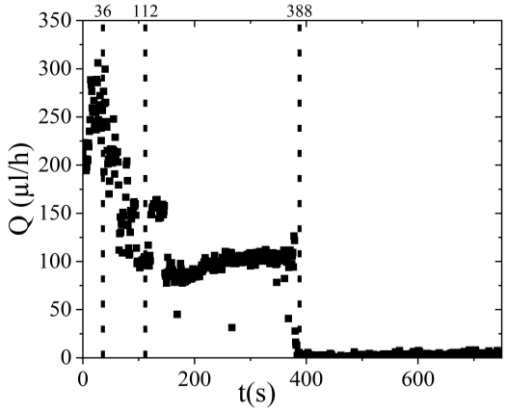

Figure 21. Temporal evolution of flow rate Q when 0.8 wt% of microgel-25µm is flowed through the Lateral-20 porous channel. The flow is pressure-controlled with P_1= 40 mbar, P_2= 20 mbar and P_3= 10 mbar. The dotted lines correspond to the times at which three of the pictures in Figure 20 are taken.

We have performed experiments with other sets of pressures (P_1, P_2, P_3); they all show a similar build-up of a microgel filter cake in the lateral arm of the channel, which progressively helps prevent the loss of fluid.

Discussion.

These experiments show that the same mechanism is at play as in frontal filtration experiments. Whereas the semidilute microgel behaves like a Newtonian fluid of low viscosity in the main channel, the microgel particles aggregate when entering the microchannels and form a jammed material. The progressive extrusion of this gel-like jammed material from the pores to the lateral arm eventually leads to the formation of a filter cake that completely covers the porous medium, finally preventing flow leakage from the main channel to the

lateral arm. As discussed in the previous section, this jamming behavior is likely an extensional-shear-induced aggregation process. It should be noted that the extensional shear rate in the lateral filtration experiments is of the same order as in the frontal filtration experiments.

4. Conclusion

The flow behavior of associative microgel particles in simple shear flow is seen to be well described by a power-law model up to a concentration of the order of 7 wt%. Beyond this concentration, the microgel suspension has a yield stress and is described by the Herschel-Bulkley model. We show that a phase diagram and the jamming fraction are obtained by a simple experiment consisting of imaging the drying of a microgel droplet. Our results on the jamming concentration are consistent with the results obtained from the bulk rheology; the maximum particle fraction reached under drying is consistent with that reached in high-pressure filtration experiments. In model porous media for frontal filtration, we show the progressive jamming of the initially semi-dilute microgel suspension, which forms aggregates and eventually a gel-like mass after passing through the pores. The filter cake thus *grows at the exit* of the pores, which contrasts with the classical picture of cake formation. Because flow in a linear channel of the same size as the pore size does not lead to any jamming, jamming is explained in terms of an extensional-shear-induced aggregation of the suspension when it undergoes a high extensional shear at the entrance of the pores. By unfolding the dangling chains of microgel particles, as observed for the aggregation of proteins in the literature[52], extensional flows could indeed favor the association between hydrophobic groups of chains belonging to different particles. In porous media for lateral filtration, a filter cake builds up with the same mechanism and leads to fluid loss control. The filter cakes formed through this process have low permeability. Interestingly, the extensional-flow-induced aggregation of associative microgel particles confers self-adaptive properties of the fluid loss additive with respect to the pore network to be clogged. Indeed, aggregated gels larger than the individual microgels can form and be used to limit fluid loss even if the pore size is larger than the microgel particles. An interesting feature of these aggregates formed under extensional shear is that they are not reversible once flow stops; large gel objects remain within the filter structure and retain their ability to seal the porous section permanently.

5. Acknowledgments

The authors thank Arnaud Cadix from Syensqo for providing the microgels and for fruitful discussions.

References

1. Fink J. *Petroleum Engineer's Guide to Oil Field Chemicals and Fluids*. Gulf Professional Publishing; 2015.
2. Saunders BR, Vincent B. Microgel particles as model colloids: theory, properties and applications. *Advances in Colloid and Interface Science*. 1999;80(1):1-25.
3. Moulin E. Fluid loss control agents and compositions for cementing oil wells comprising said fluid loss control agent. Google Patents; 2001.
4. Ezell RG, Wu JJ. Methods of using fluid loss additives comprising micro gels. Google Patents; 2014.
5. Zweigle ML, Lamphere JC. Cross-linked, water-swellable polymer microgels. Google Patents; 1979.
6. Zaitoun A, Tabary R, Rousseau D, et al. Using microgels to shut off water in a gas storage well. Society of Petroleum Engineers; 2007:
7. Rousseau D, Tabary R, Zaitoun A, Pichery T, Mallo P, Braun O. New Microgels for EOR–From Laboratory to Field Applications. 2007:
8. Tran‐Viet A, Routh AF, Woods AW. Control of the permeability of a porous media using a thermally sensitive polymer. *AIChE Journal*. 2014;60(3):1193-1201.
9. Mewis J, Wagner NJ. Current trends in suspension rheology. *Journal of Non-Newtonian Fluid Mechanics*. 2009/04/01/ 2009;157(3):147-150.
10. Senff H, Richtering W. Temperature sensitive microgel suspensions: Colloidal phase behavior and rheology of soft spheres. *The Journal of Chemical Physics*. 1999/07/22 1999;111(4):1705-1711.
11. Tan BH, Pelton RH, Tam KC. Microstructure and rheological properties of thermo-responsive poly(N-isopropylacrylamide) microgels. *Polymer*. 2010/06/24/ 2010;51(14):3238-3243.
12. Tan BH, Tam KC, Lam YC, Tan CB. Microstructure and rheological properties of pH-responsive core–shell particles. *Polymer*. 2005/11/14/ 2005;46(23):10066-10076.
13. Borrega R, Cloitre M, Betremieux I, Ernst B, Leibler L. Concentration dependence of the low-shear viscosity of polyelectrolyte micro-networks: From hard spheres to soft microgels. *EPL (Europhysics Letters)*. 1999;47(6):729.
14. Stokes JR, Frith WJ. Rheology of gelling and yielding soft matter systems. 10.1039/B719677F. *Soft Matter*. May 14 2008;4(6):1133-1140.
15. De Gennes P-G. *Scaling concepts in polymer physics*. Cornell university press; 1979.
16. Israelachvili JN. *Intermolecular and Surface Forces*. Intermolecular and Surface Forces. Academic Press; 2011.
17. Marshall RJ, Metzner AB. Flow of Viscoelastic Fluids through Porous Media. *Industrial & Engineering Chemistry Fundamentals*. 1967/08/01 2002;6(3):393-400.
18. Sadowski TJ, Bird RB. Non-Newtonian Flow through Porous Media. I. Theoretical. *Transactions of the Society of Rheology*. 1965/09/01 1965;9(2):243-250.
19. Savins JG. Non-Newtonian Flow through Porous Media. *Industrial & Engineering Chemistry*. 1969/10/01 2002;61(10):18-47.
20. Bird RB. Chemical engineering education: a gallimaufry of thoughts. *Annu Rev Chem Biomol Eng*. 2010/06/15 2010;1(1):1-17.
21. James DF, McLaren DR. The laminar flow of dilute polymer solutions through porous media. *Journal of Fluid Mechanics*. 2006;70(4):733-752.

22. Kulicke WM, Haas R. Flow behavior of dilute polyacrylamide solutions through porous media. 1. Influence of chain length, concentration, and thermodynamic quality of the solvent. *Industrial & Engineering Chemistry Fundamentals*. 1984/08/01 2002;23(3):308-315.
23. Li Y, Dai C, Wu Y, Xu K, Zhao M, Wang Y. Viscoelastic surfactant fluids filtration in porous media: A pore‐scale study. *AIChE Journal*. 2020;66(6):e16229.
24. Ferer M, Ji C, Bromhal GS, Cook J, Ahmadi G, Smith DH. Crossover from capillary fingering to viscous fingering for immiscible unstable flow:Experiment and modeling. *Phys Rev E Stat Nonlin Soft Matter Phys*. 07/08/ 2004;70(1 Pt 2):016303.
25. Perrin CL, Tardy PM, Sorbie KS, Crawshaw JC. Experimental and modeling study of Newtonian and non-Newtonian fluid flow in pore network micromodels. *J Colloid Interface Sci*. Mar 15 2006;295(2):542-50.
26. Wyss HM, Blair DL, Morris JF, Stone HA, Weitz DA. Mechanism for clogging of microchannels. *Phys Rev E Stat Nonlin Soft Matter Phys*. Dec 2006;74(6 Pt 1):061402.
27. Haw MD. Jamming, Two-Fluid Behavior, and "Self-Filtration" in Concentrated Particulate Suspensions. *Physical review letters*. 2004;92:185506.
28. Dressaire E, Sauret A. Clogging of microfluidic systems. *Soft matter*. 2017;13:37-48.
29. Moore CP, Husson J, Boudaoud A, Amselem G, Baroud CN. Clogging of a Rectangular Slit by a Spherical Soft Particle. *Phys Rev Lett*. Feb 10 2023;130(6):064001.
30. Tung KL, Chen LH, Chen YR, Lin YS, Lin YF, Li YL. Fluid flow through compressible soft particle beds. *AIChE Journal*. 2016;62(5):1716-1727.
31. Luken A, Stuwe L, Lohaus J, Linkhorst J, Wessling M. Particle movements provoke avalanche-like compaction in soft colloid filter cakes. *Sci Rep*. Jun 18 2021;11(1):12836.
32. Kaushik S. *Filtration mechanism of suspensions of microgels*. Université de Bordeaux; 2019. https://tel.archives-ouvertes.fr/tel-02152640
33. Clement F, Leng J. Evaporation of liquids and solutions in confined geometry. *Langmuir*. Aug 3 2004;20(16):6538-41.
34. Bhattacharya S, Datta A, Berg JM, Gangopadhyay S. Studies on surface wettability of poly(dimethyl) siloxane (PDMS) and glass under oxygen-plasma treatment and correlation with bond strength. *Journal of Microelectromechanical Systems*. 2005;14(3):590-597.
35. Morra M, Occhiello E, Marola R, Garbassi F, Humphrey P, Johnson D. On the aging of oxygen plasma-treated polydimethylsiloxane surfaces. *Journal of Colloid and Interface Science*. 1990/06/01/ 1990;137(1):11-24.
36. Makamba H, Kim JH, Lim K, Park N, Hahn JH. Surface modification of poly(dimethylsiloxane) microchannels. *Electrophoresis*. Nov 2003;24(21):3607-19.
37. Decock J. *Approches micro/milli-fluidiques pour l'étude in situ de procédés de filtration frontale*. 2017. http://www.theses.fr/2017BORD0788/document
38. Duffy DC, McDonald JC, Schueller OJ, Whitesides GM. Rapid Prototyping of Microfluidic Systems in Poly(dimethylsiloxane). *Anal Chem*. Dec 1 1998;70(23):4974-84.
39. Goehring L, Clegg WJ, Routh AF. Plasticity and fracture in drying colloidal films. *Phys Rev Lett*. Jan 11 2013;110(2):024301.
40. Ziane N, Salmon JB. Solidification of a Charged Colloidal Dispersion Investigated Using Microfluidic Pervaporation. *Langmuir*. Jul 28 2015;31(29):7943-52.
41. Bouchaudy A, Salmon JB. Drying-induced stresses before solidification in colloidal dispersions: In situ measurements. *Soft Matter*. 2019;15:2768-2781.
42. Guazzelli É, Pouliquen O. Rheology of dense granular suspensions. *Journal of Fluid Mechanics*. 2018;852:P1.
43. Mason TG, Bibette J, Weitz DA. Yielding and Flow of Monodisperse Emulsions. *Journal of Colloid and Interface Science*. 1996/05/10/ 1996;179(2):439-448.
44. Lobry L, Lemaire E, Blanc F, Gallier S, Peters F. Shear thinning in non-Brownian suspensions explained by variable friction between particles. *Journal of Fluid Mechanics*. 2018;860:682-710.
45. Gilbert D, Valette R, Lemaire E. Impact of particle stiffness on shear-thinning of non-Brownian suspensions. *Journal of Rheology*. 2022;66(1):161-176.

46. Lemaire E, Blanc F, Claudet C, Gallier S, Lobry L, Peters F. Rheology of non-Brownian suspensions: a rough contact story. *Rheologica Acta*. 2023/06/01 2023;62(5-6):253-268.
47. Rouyer F, Pitois O, Lorenceau E, Louvet N. Permeability of a bubble assembly: from the very dry to the wet limit. *Physics of Fluids*. 2010;22:043302.
48. Meeker SP, Bonnecaze RT, Cloitre M. Slip and flow in pastes of soft particles: Direct observation and rheology. *Journal of Rheology*. 2004;48(6):1295-1320.
49. Xie D, Wu H, Zaccone A, Braun L, Chen H, Morbidelli M. Criticality for shear-induced gelation of charge-stabilized colloids. 10.1039/C002043E. *Soft Matter*. 2010;6(12):2692-2698.
50. Wu H, Zaccone A, Tsoutsoura A, Lattuada M, Morbidelli M. High shear-induced gelation of charge-stabilized colloids in a microchannel without adding electrolytes. *Langmuir*. Apr 21 2009;25(8):4715-23.
51. Sendekie ZB, Bacchin P. Colloidal Jamming Dynamics in Microchannel Bottlenecks. *Langmuir*. Feb 16 2016;32(6):1478-88.
52. Dobson J, Kumar A, Willis LF, et al. Inducing protein aggregation by extensional flow. *Proc Natl Acad Sci U S A*. May 2 2017;114(18):4673-4678.